Annals of Glaciology

Article

Cite this article: Tian Z, Liang X, Zhao F, Liu N, Li M, Li C (2024). On the effects of the timing of an intense cyclone on summertime sea-ice evolution in the Arctic. *Annals of Glaciology* 1–15. https://doi.org/10.1017/aog.2024.15

Received: 9 October 2023
Revised: 30 March 2024
Accepted: 8 April 2024

Keywords:
Arctic; cyclone; heat budget; sea-ice volume

Corresponding author:
Xi Liang;
Email: liangx@nmefc.cn

cambridge.org/aog

On the effects of the timing of an intense cyclone on summertime sea-ice evolution in the Arctic

Zhongxiang Tian, Xi Liang, Fu Zhao, Na Liu, Ming Li and Chunhua Li

Key Laboratory of Marine Hazards Forecasting, National Marine Environmental Forecasting Center, Ministry of Natural Resources, Beijing, China

Abstract

This study investigates the impacts of the timing of an extreme cyclone that occurred in August 2012 on the sea-ice volume evolution based on the Arctic Ice Ocean Prediction System (ArcIOPS). By applying a novel cyclone removal algorithm to the atmospheric forcing during 4–12 August 2012, we superimpose the derived cyclone component onto the atmospheric forcing one month later or earlier. This study finds that although the extreme cyclone leads to strong sea-ice volume loss in all runs, large divergence occurs in sea-ice melting mechanism in response to various timing of the cyclone. The extreme cyclone occurred in August, when enhanced ice volume loss is attributed to ice bottom melt primarily and ice surface melt secondarily. If the cyclone occurs one month earlier, ice surface melt dominates ice volume loss, and earlier appearance of open water within the ice zone initiates positive ice-albedo feedback, leading to a long lasting of the cyclone-induced impacts for approximately one month, and eventually a lower September ice volume. In contrast, if the cyclone occurs one month later, ice bottom melt entirely dominates ice volume loss, and the air-open water heat flux in the ice zone tends to offset ice volume loss.

1. Introduction

With the shrinking and thinning of Arctic sea-ice cover (Bi and others, 2018; Kwok, 2018; Simmonds and Li, 2021), the Arctic Ocean is occupied by more and more seasonal sea ice (Hao and others, 2020). Seasonal sea ice, normally with small thickness and low strength, changes more rapidly and drastically in response to strong cyclones (Lukovich and others, 2021). Several studies have suggested that summertime intense cyclones affect the local sea-ice concentration (Kriegsmann and Brümmer, 2014; Clancy and others, 2022) and the September sea-ice extent minima (Serreze and others, 2003; Screen and others, 2011; Lukovich and others, 2021). Arctic intense cyclones have great impacts on the ever-increasing human activities in the Arctic due to the accompanied extreme weather, such as high winds and precipitation.

The physical mechanisms of cyclones affecting sea ice have been widely studied. Cyclone-induced strong and inhomogeneous wind promotes sea-ice deformation leading to sea-ice leads and polynyas. Shortwave radiation absorbed by sea-ice leads and polynyas accelerates local sea-ice melt via the positive ice/snow albedo feedback (Kriegsmann and Brümmer, 2014). Wind-driven sea waves cause sea-ice fracture at marginal ice zone, further promoting sea-ice lateral melt. Besides, strong wind drives sea ice moving quickly, stirs the upper ocean powerfully and results in elevated upper ocean vertical mixing, which warms the cold ocean surface in ice zone (Jackson and others, 2012) and leads to enhanced oceanic heat flux at the ice base (Zhang and others, 2013; Stern and others, 2020; Tian and others, 2022). On the east side of cyclone's trajectory, cyclone-induced wind brings relatively warm and moist air from low latitudes to high latitudes, while on the west side of cyclone's trajectory, relatively cool and dry air from high latitudes is advected to low latitudes, thus enhanced turbulent heat flux and sea-ice surface melt occur on the east side of the cyclone (Clancy and others, 2022). Statistically, many studies have pointed out that summer cyclones promote sea-ice loss in the Atlantic Arctic (e.g., Kriegsmann and Brümmer, 2014; Semenov and others, 2019) due to the enhanced sea-ice export via Fram Strait, while promote sea-ice loss in the Pacific Arctic due to the combined thermodynamical and dynamical effects originating from the vulnerability of thin ice to wind forcing (Semenov and others, 2019). However, Schreiber and Serreze (2020) revealed that summer cyclones impede sea-ice loss. This is because the decrement of sea-ice loss owing to cyclone-induced reductions in air temperature and shortwave radiation counteracts the increment of sea-ice loss owing to cyclone-induced elevated sea-ice dynamical role. Moreover, Clancy and others (2022) found that sea-ice losses on the east side of cyclones owing to more heat absorption and sea-ice divergence, and sea-ice gains on the west side of cyclones due to sea-ice convergence.

Ignoring the hard achieving of consensus on the spatial differentiation of cyclone's impact on sea ice, the temporal differentiation of cyclone's impact on sea ice has been paid little attention. Screen and others (2011) indicated that years when fewer cyclones occurred during May–July in the central Arctic tend to have lower September sea-ice area due to the reduced cloud cover, enhanced transpolar drift and strengthened background anticyclonic winds. Finocchio

and others (2020) conducted a more detailed study using ERA5 reanalysis data. They analyzed the thermodynamical and dynamical effects of cyclones occurring during May–August on local sea-ice evolution in the marginal ice zone, and concluded that cyclones occurring in May and June impede the seasonal loss of sea-ice extent mainly due to the reduction of net shortwave radiation heat flux at the surface, while cyclones occurring in July and August promote sea-ice extent loss due to the enhanced upper ocean mixing, the warm air advection associated with long-lived cyclones and the strong response of thin ice dynamical processes in late summer. Finocchio and others (2022) further demonstrated that the 1–7 day losses in sea-ice area and thickness following August cyclone days have increased in 2009–2018 with respect to 1991–2000. This phenomenon is most evident in the Amerasian Arctic where the average upper-ocean temperature has increased by 0.2–0.8°C and the average ice thickness has decreased by almost 1 m between the two decades, which allows the elevation of cyclone-induced ocean mixing and sea-ice divergence. In contrast, June cyclones in both decades locally slowdown seasonal sea-ice loss, and the recent increase in sea-ice loss following non-cyclone conditions in June primarily occurs in the Eurasian sector, where substantial reductions in average surface albedo in the recent decade have allowed more of the abundant insolation in the absence of cyclones to arrive the ocean surface. Lukovich and others (2021) proposed that cyclone-induced sea-ice extent loss depends on the timing and location of the cyclone by analyzing the effects of the two intense cyclones occurred in August 2012 and August 2016 on sea-ice evolution. Aue and Rinke (2023) proved the impacts of cyclones on sea-ice conditions in the Atlantic Arctic strongly vary both in space and time, with intimate relation to the initial sea-ice conditions and the cyclone intensity.

Due to the limitation of polar observations, reanalysis data and analysis methods in most previous studies, the influences of different cyclones' strengths and trajectories on sea-ice evolution are rarely isolated. Thus, a view on the impact of the different timing of a given cyclone on summer sea ice is missing. In this study, we combine a novel cyclone isolation and extraction algorithm and an Arctic ice–ocean coupled modeling system to address this knowledge gap to improve understanding on rapid changes in Arctic sea ice. 'The Great Arctic Cyclone of August 2012' (Simmonds and Rudeva, 2012) is selected and the 3-hourly Japanese 55-year Reanalysis data (JRA55) are used. We apply the novel cyclone removal method described in Tian and others (2022) to the JRA55 data during 4–12 August 2012 to derive the intense cyclone component, then we superimpose the intense cyclone component onto the JRA55 data during 4–12 July 2012, and 4–12 September 2012, respectively. Using the modified JRA55 data to drive the model, we conduct four numerical experiments to study the thermodynamical and dynamical influences of the timing of the cyclone on sea-ice evolution. This procedure of moving the cyclone component to another period in an atmospheric reanalysis data effectively keeps the cyclone's trajectory and strength unchanged. The paper is organized as follows: section 2 describes the modeling system and the numerical experiments. Section 3 presents sea-ice volume (SIV) and heat flux budget analysis in numerical experiments and analyzes sea-ice evolution in response to different timing of the cyclone. Discussion and conclusions are given in section 4.

2. Model and numerical experiments

2.1. Arctic ice ocean prediction system

In this study, we use the Arctic Ice Ocean Prediction System (ArcIOPS) to conduct numerical experiments. The ArcIOPS is an ensemble synoptic-scale sea-ice forecasting system with an ensemble size of 12, operationally running at the National Marine Environmental Forecasting Center of China. The system consists of an Arctic configuration of the Massachusetts Institute of Technology General Circulation Model (MITgcm; Marshall and others, 1997) and an ensemble Kalman filter (EnKF) data assimilation model, which is configured on the Parallel Data Assimilation Framework (PDAF; Nerger and others, 2012). The horizontal grid cells are 420×384 with an averaged resolution of 18 km. The open boundaries near 55°N both on the Pacific and Atlantic sectors. In the ArcIOPS, the sea-ice model uses zero-layer snow/ice thermodynamics and viscous-plastic dynamics (Hibler, 1980), and ocean model uses a seventh-order monotonicity-preserving advection scheme (Daru and Tenaud, 2004), K-profile parameterization vertical mixing scheme (Large and others, 1994) and bulk formula (Doney and others, 1998) for surface heat flux calculation. The ocean model has 50 uneven vertical levels, with the highest vertical resolution of 10 m in the upper 100 m. Seven atmospheric parameters are needed to drive the ArcIOPS, including 2 m air temperature, 2 m specific humidity, 10 m wind speed components (u and v), downward shortwave and longwave radiation at sea surface and precipitation.

2.2. Numerical experiments

Intense Arctic cyclone in summer 2012 formed on 2 August over Siberia, moved into the Arctic Ocean on 4 August through the East Siberian Sea, its central pressure reached the minimum value of 965 hPa on 6 August (Fig. 1d) over the Canadian Basin, and then weakened gradually and dissipated on 15 August over the Canadian Arctic Archipelago. The central pressure of the cyclone rose to 1002 hPa at 00UTC 13 August (Fig. 1d); thereafter its ability to impact sea ice and ocean greatly attenuated, thus we select the period of 4–12 August as the active period of the cyclone. The method to derive the intense cyclone component from the JRA55 data has been described in Tian and others (2022) in detail. The basic idea of the novel cyclone removal method includes: (1) find the central position of the cyclone by searching for the minimum air surface pressure; (2) get the approximate extent of the cyclone using the positions of the outermost closed isobar; (3) determine the accurate extent of the cyclone by checking the tangential wind component in a polar coordinate system; (4) isolate the cyclone component from the anomalous field in all the model-required atmospheric forcing variables using a nine-point smoothing operator iteratively over the accurate extent of the cyclone. Figure 1 shows the real atmospheric state (Fig. 1a), the derived cyclone component (Fig. 1c) and the derived atmospheric state without the cyclone component (Fig. 1b) in the JRA55 data at 12UTC 6 August 2012. It is noteworthy that the cyclone removal algorithm is applied to all time layers in the JRA55 data between 00UTC 4 August 2012 and 21UTC 12 August 2012.

Initialized from the ensemble historical restart files on 1 January 2012, the ArcIOPS is integrated to 28 June 2012, and the ensemble restart files at 00UTC 29 June 2012 are saved to use in the four numerical experiments. To lay a good foundation for the four numerical experiments, satellite-retrieved daily sea-ice concentration (SIC) and sea surface temperature (SST) data in ice-free regions before 28 June 2012, and two kinds of observed sea-ice thickness data before 15 April 2012 are assimilated into the system. The SIC observations, derived from the Special Sensor Microwave Imager Sounder (SSMIS) brightness temperature data, are daily provided by the University of Hamburg (Kaleschke and others, 2001; Cavalieri and others, 2011). The

https://doi.org/10.1017/aog.2024.15 Published online by Cambridge University Press

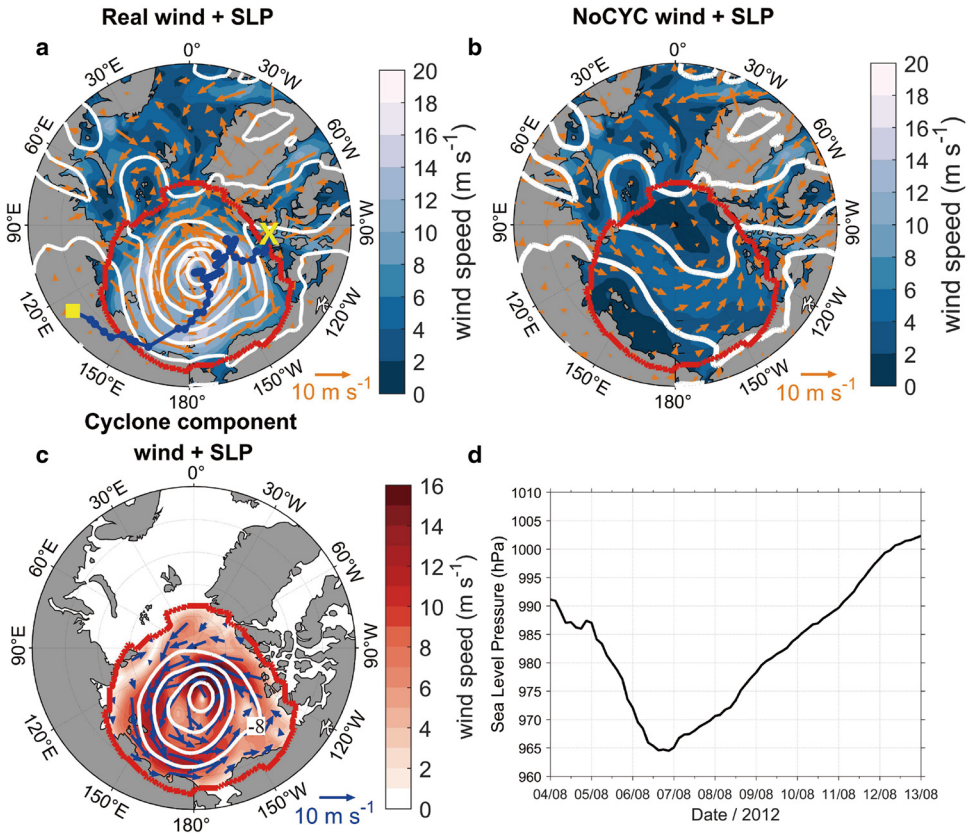

Figure 1. Spatial distributions of sea level pressure (SLP) and 10 m wind speed at 12UTC 6 August 2012 in (a) the original JRA55 data, (b) the modified JRA55 data with the removal of the cyclone component and (c) the derived cyclone component. Wind speed is shaded. White lines denote SLP with an interval of 8 hPa. Red lines denote the cyclone's extent at 12UTC 6 August. Blue line in (a) denotes the cyclone's trajectory between 00UTC 4 August and 00UTC 13 August. Blue dots in (a) indicate the central positions of the cyclone, with a time interval of 3 h. Yellow square and 'x' in (a) represent the central positions of the cyclone at 00UTC 4 August and 00UTC 13 August, respectively. (d) Time series of the central pressure of the cyclone during 4–12 August.

SST observations, derived from the Group for High-Resolution SST Multi-Product Ensemble (GMPE) SST data, are daily provided by the United Kingdom Met Office (UKMO) (Martin and others, 2012). Daily sea-ice thickness observations in thin ice zones (<1 m), derived from the Soil Moisture Ocean Salinity (SMOS) brightness temperature data (Tian-Kunze and others, 2014), are assimilated on a daily basis. Weekly sea-ice thickness observations, derived from the European Space Agency satellite mission CryoSat-2 radar altimetric measurements (Laxon and others, 2013; Ricker and others, 2014), are assimilated every 7 days.

Restarted from the ensemble restart files at 00UTC 29 June 2012, we design four experiments without any data assimilation to obtain more realistic simulation results. The four experiments have the same configuration except the atmospheric forcing. The first experiment, denoted by CYC8, uses the 3-hourly JRA-55 data from 00UTC 29 June 2012 to 00UTC 1 October 2012 to drive the ArcIOPS. The second experiment, denoted by NoCYC, uses the same JRA-55 data from 00UTC 29 June 2012 to 00UTC 1 October 2012 but with the removal of the cyclone component from 00UTC 4 August 2012 to 00UTC 13 August 2012. The other two experiments, denoted by CYC7 and CYC9, use the same JRA-55 data from 00UTC 29 June 2012 to 00UTC 1 October 2012 but with moving the cyclone component to one month earlier and later, respectively. Six-hourly model output from 29 June to 1 October are saved in all experiments and used in our analysis. Comparison between the four experiments reveals the influence of the timing of the cyclone on the summertime minimum SIV. We conduct the following analyses for the whole Arctic region (north of 60°N), owing to the wide coverage of the selected intense cyclone in this study.

It has been proved that the ArcIOPS has a reliable performance on simulating the Arctic sea-ice spatial distribution both for concentration and for thickness (Liang and others, 2019, 2020; Mu and others, 2019), and on simulating sea-ice evolution in response to the intense Arctic cyclone in August 2012 (Tian and others, 2022). SIV evolution in the CYC8 run, which is driven by the original atmospheric forcing, generally agrees with that derived from the Pan-Arctic Ice Ocean Modeling and Assimilation System (PIOMAS; Zhang and Rothrock, 2003). Especially during the active period of the cyclone, both the SIV loss rates in the CYC8 run and the PIOMAS show rapid increases along with intensification of the cyclone (black line vs. pink line in Fig. 2d). Further validation of the CYC8 run against observations can be referred to Table 1 in Tian and others (2022).

3. Result

3.1. Sea-ice volume budget analysis

The ArcIOPS divides each gridcell into two parts: the ice-covered area and the open water area. SIV evolution in each gridcell is determined by the atmospheric heat flux at the ice surface, the atmospheric heat flux at the open water area, the oceanic heat flux at the ice bottom, sea-ice advection and snow flooding process. The atmospheric heat flux at the open water area in the sea-ice zone is used to melt sea ice in local gridcell first, then warm the surface ocean gridcell after no ice survived.

Following Liang and others (2022), the change of sea-ice volume (ΔSIV) in a given region with area S over a period t can be described as:

$$\Delta \mathrm{SIV} = V_{\mathrm{io}} + V_{\mathrm{ai}} + V_{\mathrm{ao}} + V_{\mathrm{fl}} + V_{\mathrm{adv}} + R_{\mathrm{V}} \quad (1)$$

https://doi.org/10.1017/aog.2024.15 Published online by Cambridge University Press

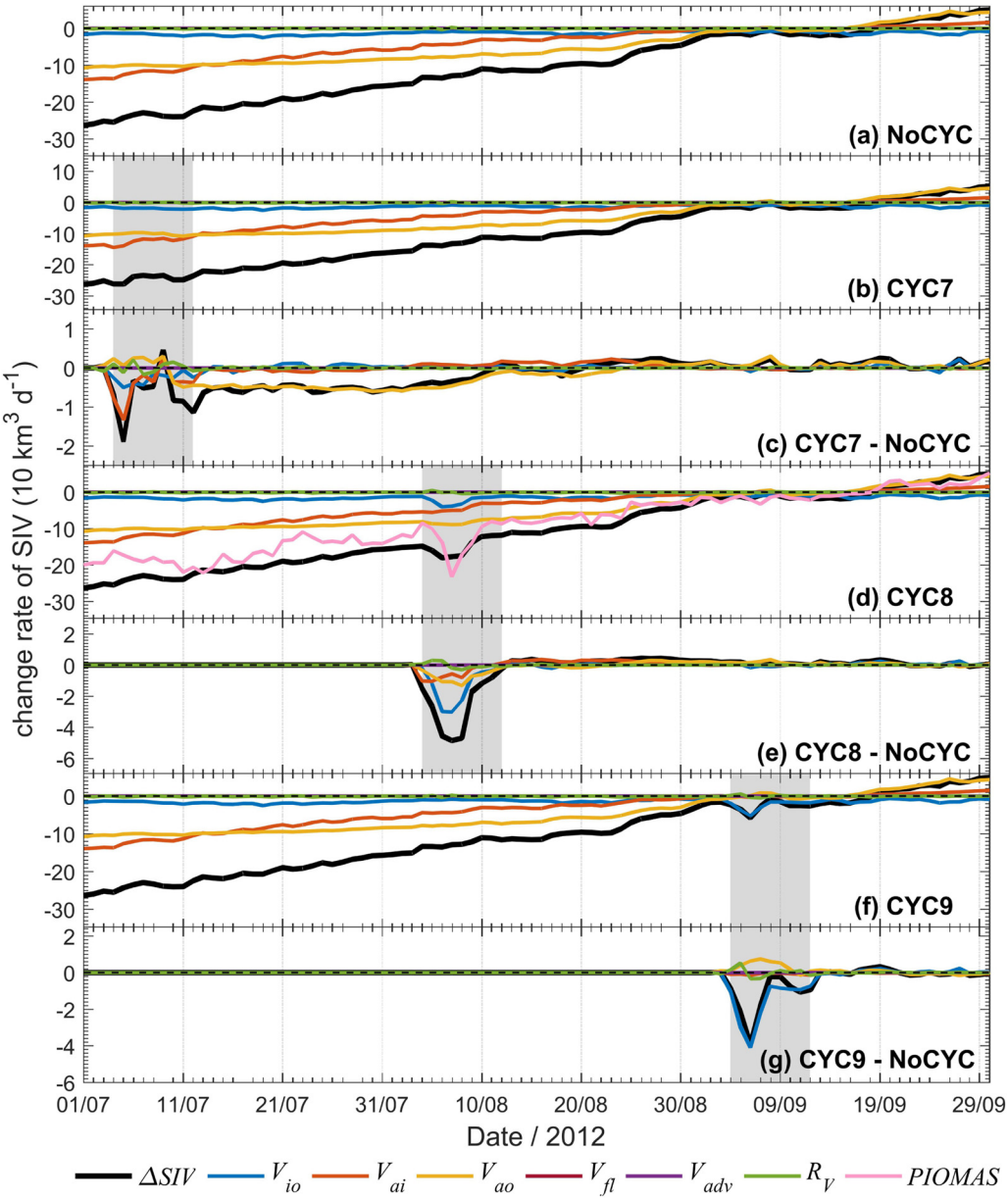

Figure 2. Change rate of sea-ice volume (SIV) integrated over the entire Arctic Ocean in (a) the NoCYC run, (b) the CYC7 run, (d) the CYC8 run, (f) the CYC9 run and the differences between (c) the CYC7, (e) the CYC8, (g) the CYC9 and the NoCYC runs. The black, blue, orange, yellow, claret, purple and green lines represent the ΔSIV, V_{io}, V_{ai}, V_{ao}, V_{fl}, V_{adv} and R_v, respectively. The active period of the cyclone is shaded by light gray. Negative values in (c), (e) and (g) mean loss of SIV in the CYC7, CYC8 and CYC9 runs is stronger than that in the NoCYC run, respectively.

where V_{io}, V_{ai} and V_{ao} are the change of SIV due to the oceanic heat flux at the ice bottom, the atmospheric heat flux at the ice surface and the atmospheric heat flux at the open water area, respectively. V_{fl} represents the contribution of snow flooding process to the increase of SIV. V_{adv} is the contribution of advection on SIV. R_v can be calculated as residual term and only includes small computational error which is always nearly zero. V_{io}, V_{ai}, V_{ao} and V_{fl} could be calculated by the integral of the change rate of cell-mean sea-ice thickness (θ_{io}, θ_{ai}, θ_{ao}, θ_{fl}) in each gridcell over time t and cell area s, that is, $V_* = \iint \theta_* \, dtds$, and $V_{adv} = \iint (\partial\phi_{advx}/\partial x + \phi_{advy}/\partial y) \, dtds$, in which ($\phi_{advx}$, ϕ_{advy}) are the components of advection of cell-mean sea-ice thickness. Variables (θ_{io}, θ_{ai}, θ_{ao}, θ_{fl}, ϕ_{advx}, ϕ_{advy}) are directly saved by the model every 6 h.

The intense cyclone greatly accelerates sea-ice melting during the active period of the cyclone in the CYC7, CYC8 and CYC9 runs (Fig. 2). V_{fl} is close to zero in all runs (Figs 2a, b, d, f) due to the weak snow flooding process in the Arctic (Graham and others, 2019), particularly in summer. V_{adv} is also zero in all runs, because our control region covers the whole Arctic sea-ice zone in summertime, so no net sea-ice advection across the boundary of the control region occurs.

In the CYC7 and NoCYC runs, the open water area in the sea-ice zone is small with respect to ice-cover area before 12 July (Figs 3a, b), so the atmospheric heat flux at the ice-covered area contributes more in SIV loss than other terms, i.e. the SIV loss due to V_{ai} is larger than other terms (orange lines in Figs 2a, b). However, along with the expanding of open water area in sea-ice zone after 12 July (Figs 3a, b), the atmospheric heat flux at the open water area results in more sea-ice melting, and SIV loss due to V_{ao} contributes the largest to total SIV loss in late July and throughout August (yellow lines in Figs 2a, b). In the CYC7 run (Fig. 2b), the largest SIV melting rate occurs on 5 July, with a magnitude of 261.8 $km^3\ d^{-1}$, in which the cyclone contributes 18.9 $km^3\ d^{-1}$ (Fig. 2c). The cyclone-induced warm and moist air (Supplementary Fig. S1) accelerates heat exchange at the air–ice interface leading to large SIV loss due

https://doi.org/10.1017/aog.2024.15 Published online by Cambridge University Press

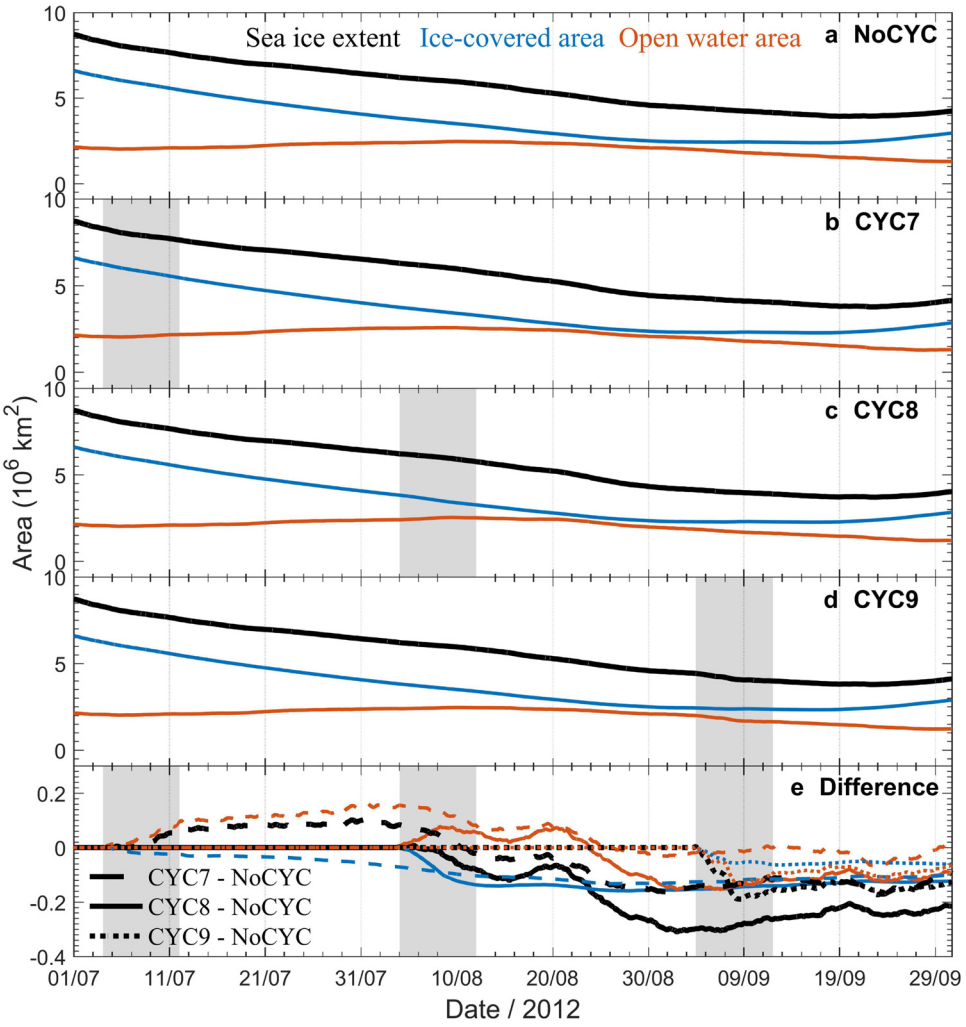

Figure 3. Time series of sea-ice extent (the sum of gridcell areas of cells with >0% sea-ice concentration; black lines), ice-covered area (blue lines) and open water area in sea-ice zone (orange lines) in (a) the NoCYC run, (b) the CYC7 run, (c) the CYC8 run, (d) the CYC9 run and (e) the differences between the CYC7, CYC8, CYC9 and NoCYC runs. Positive values in (e) mean the term in the CYC7, CYC8 or CYC9 runs is larger than that in the NoCYC run.

to the V_{ai} term. However, sea ice is concentrated and thick in early July, so the cyclone-induced strong wind is not able to efficiently break the ice pack and disturb the upper ocean. Thus, SIV loss due to the V_{io} term grows moderately. The cyclone-induced SIV loss is 62.7 km^3 during the active period of the cyclone, while the contributions of V_{ai} and V_{io} are 38.7 and 24.8 km^3, respectively (Fig. 2c). The cyclone-induced expansion of open water area in the sea-ice zone in the CYC7 run (Figs 3a, b, e) allows the positive ice/snow albedo feedback to function for a long time in the rest of summertime, leading to an enhanced sea-ice melting rate until 10 August in the CYC7 run. The cyclone-induced SIV loss due to θ_{ao} accumulates up to 143.2 km^3 from 13 July to 10 August. In summary, the influence of a cyclone occurring in early July on sea ice could last for one month.

The difference between the CYC8 and NoCYC runs (Fig. 2e) shows that the cyclone's contributions to SIV loss in descending order are V_{io}, V_{ao} and V_{ai} during the active period of the cyclone. SIC is lower on average in August compared to July, creating advantage for the transfer of wind momentum into the ocean in sea-ice zone to stir the upper ocean, thus the cyclone-induced SIV loss due to V_{io} contributes the largest to total SIV loss (blue line in Fig. 2e). Meanwhile, the cyclone promotes heat exchange between atmosphere and the underlying surface, resulting in noticeable increase of SIV loss due to V_{ao} and V_{ai}. During 4–12 August, the cyclone-induced SIV loss reaches 221.9 km^3, in which V_{io}, V_{ao} and V_{ai} contribute 113.4, 63.3 and 43.3 km^3, respectively.

When the cyclone occurs in early September (Fig. 2f), the cyclone-induced SIV loss is primarily a result of enhanced oceanic heat flux at the ice bottom (Fig. 2g). The maximum cyclone-induced SIV loss is 39.5 km^3 d^{-1} on 6 September (black line in Fig. 2g), in which V_{io} contributes 41.0 km^3 d^{-1} (blue line in Fig. 2g) while V_{ao} tends to impede SIV loss by a rate of 6.8 km^3 d^{-1} (yellow line in Fig. 2g). Sea-ice extent in the CYC9 run is smaller than that in the NoCYC run, and their deviation is dominated by that in the open water area in the ice zone (black and orange dotted lines in Fig. 3e). Compared to the NoCYC run, less open water area in the ice zone allows less SIV loss induced by the V_{ao} in the CYC9 run.

When the cyclone occurs in July or August, enhanced SIV loss occurs at both the surface and the bottom of the ice; however, SIV loss primarily occurs at the ice bottom when the cyclone happens in September. Among all the experiments with the cyclone, the CYC8 run generates the largest rate of SIV loss during the active period of the cyclone (Fig. 2). Nevertheless, no matter which month the cyclone occurs, it could result in a rapid SIV loss during the active period of the cyclone. The cyclone in the CYC7 run has the most long-lasting impact on the SIV loss, and leads to a lower SIV at the end of melting season comparing with other runs (Fig. 4). All the runs generate the minimum SIV on 18 September, with the values of 3.94×10^3 km^3 for the NoCYC

https://doi.org/10.1017/aog.2024.15 Published online by Cambridge University Press

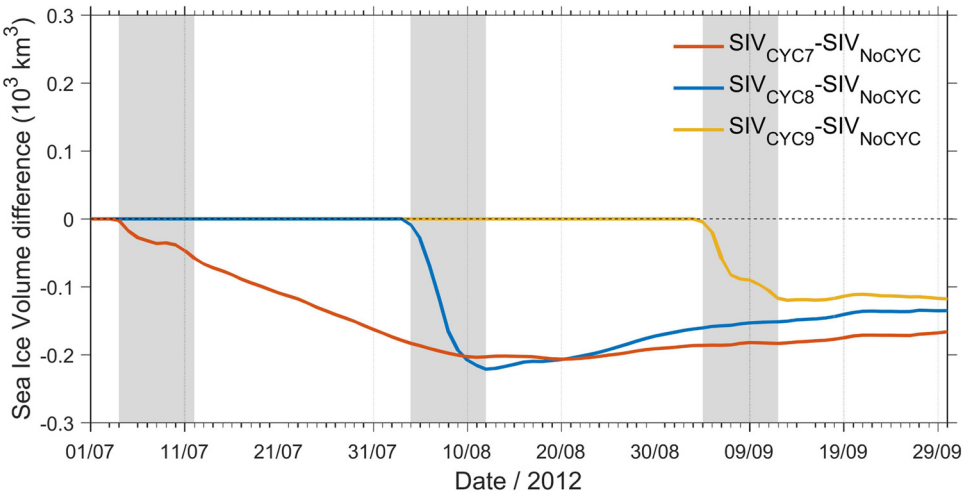

Figure 4. Time series of the deviation of the CYC7 (orange line), CYC8 (blue line) and CYC9 (yellow line) runs away from the NoCYC runs. The periods shaded by light gray denote the timing of the cyclone in different runs.

run, 3.76×10^3 km^3 for the CYC7 run, 3.79×10^3 km^3 for the CYC8 run, 3.82×10^3 km^3 for the CYC9 run. The SIV differences between the four experiments are not very large, ranging from 117 km^3 between the NoCYC and CYC9 runs, to 177 km^3 between the NoCYC and CYC7 runs.

The cyclone leads to an anti-clockwise sea-ice drift anomaly covering most regions in the Arctic Ocean for all the experiments with the cyclone (Figs 5c, 6c, 7c). In the CYC7 run, the cyclone-induced strong SIV loss locates in the Pacific Arctic, especially in areas near to the cyclone's trajectory (Figs 5a–c). SIV loss due to V_{io} is relatively large in the coastal areas in the East Siberian–Laptev Seas (Figs 5d–e), since sea ice is relatively thin in these areas allowing the cyclone-induced sea ice breaking down and thus enhanced ocean-ice heat flux. Meanwhile, enhanced SIV loss due to V_{io} also occurs in the Chukchi Cap, as well as the northern Canadian Basin although the cyclone-induced strong wind ca not efficiently break the concentrated ice pack (Figs 5d, f). SIV losses due to V_{ai} and V_{ao} happen almost in the entire Arctic, and their spatial patterns are similar in the CYC7 and NoCYC runs. SIV loss due to V_{ai} is strong in the marginal ice zone of the Pacific Arctic while that due to V_{ao} is strong in the marginal ice zone of the whole Arctic (Figs 5g, j). The cyclone-associated enhanced SIV loss due to V_{ai} occurs in the East Siberian Sea, Chukchi Sea and Beaufort Sea (Fig. 5i) while that due to V_{ao} occurs in the East Siberian Sea and the Canadian Basin (Fig. 5l). The dynamic impact of the cyclone contributes a large portion to local sea-ice changes, with SIV loss along the cyclone center track and SIV gain either side of the track (Fig. 5o). This indicates that the cyclone induces divergent sea-ice motion at the cyclone center, causing sea ice to be transported away from its center.

Comparing the CYC8 and NoCYC runs, enhanced SIV loss mainly locates in the Pacific Arctic (Figs 6a–c). The cyclone-induced strong SIV loss due to V_{io} occurs in the northwestern Beaufort Sea (Fig. 6f), and its magnitude is substantially larger than that in the CYC7 run (Fig. 5f). The mean SIC in August is lower than that in July, and less concentrated ice allows for increased wind-induced upper ocean mixing. It is noteworthy that in the marginal ice zone in the East Siberian–Chukchi–Beaufort Seas, both the V_{ai} and V_{ao} terms in the CYC8 run induce stronger SIV loss than those in the CYC7 run (Figs 5i, l, i, l). Besides, the cyclone-induced SIV loss due to V_{adv} in the CYC8 run basically shares similar pattern to that in the CYC7 run (Figs 5o, 6o).

During the active period of the cyclone, the cyclone-induced sea-ice drift anomaly is more drastic in the CYC9 run than those in other runs (Figs 5c, 6c, 7c), which can be attributed to the relatively loose and thin sea ice in September. In the CYC9 run, the cyclone-induced rapid SIV loss occurs in areas north of the Canadian Arctic Archipelago (Fig. 7c), with the largest contribution from V_{adv} (Fig. 7l). SIV changes due to V_{ao} in the CYC9 and NoCYC runs share similar pattern that SIV losses in the eastern Arctic but SIV gains in the western Arctic (Figs 7g, h). Moreover, the cyclone-associated SIV gain by V_{ao} partly neutralizes the cyclone-induced SIV loss by V_{io} in the Pacific Arctic area between 150°W and 180°W (Figs 7f, i).

3.2. Heat flux budget analysis

SIV change in an area is caused by the net heat flux at the air–ice–ocean interfaces, as well as net ice volume transport across the boundary of the area. As the previous section shows that the latter's contribution is quite small on the Arctic-wide metric analysis, we focus on heat flux in the sea-ice zone in this section. As described in section 3.1, each gridcell consists of ice-covered area and open water area in the ArcIOPS. The heat flux budget in the ice zone can be expressed as:

$$\begin{cases} \text{ice-covered area:} \quad Q_{\text{netice}} = Q_{\text{sw\_netice}} + Q_{\text{lw\_netice}} + Q_{\text{latice}} + Q_{\text{senice}} + Q_{\text{oceanic}} \\ \text{open water area:} \quad Q_{\text{netocn}} = Q_{\text{sw\_netocn}} + Q_{\text{lw\_netocn}} + Q_{\text{latocn}} + Q_{\text{senocn}} \end{cases} \tag{2}$$

where Q_{netice}, $Q_{\text{sw\_netice}}$, $Q_{\text{lw\_netice}}$, Q_{latice}, Q_{senice} and Q_{oceanic} are the total net heat flux in the ice-covered area, net shortwave radiation heat flux at the ice surface, net longwave radiation heat flux

https://doi.org/10.1017/aog.2024.15 Published online by Cambridge University Press

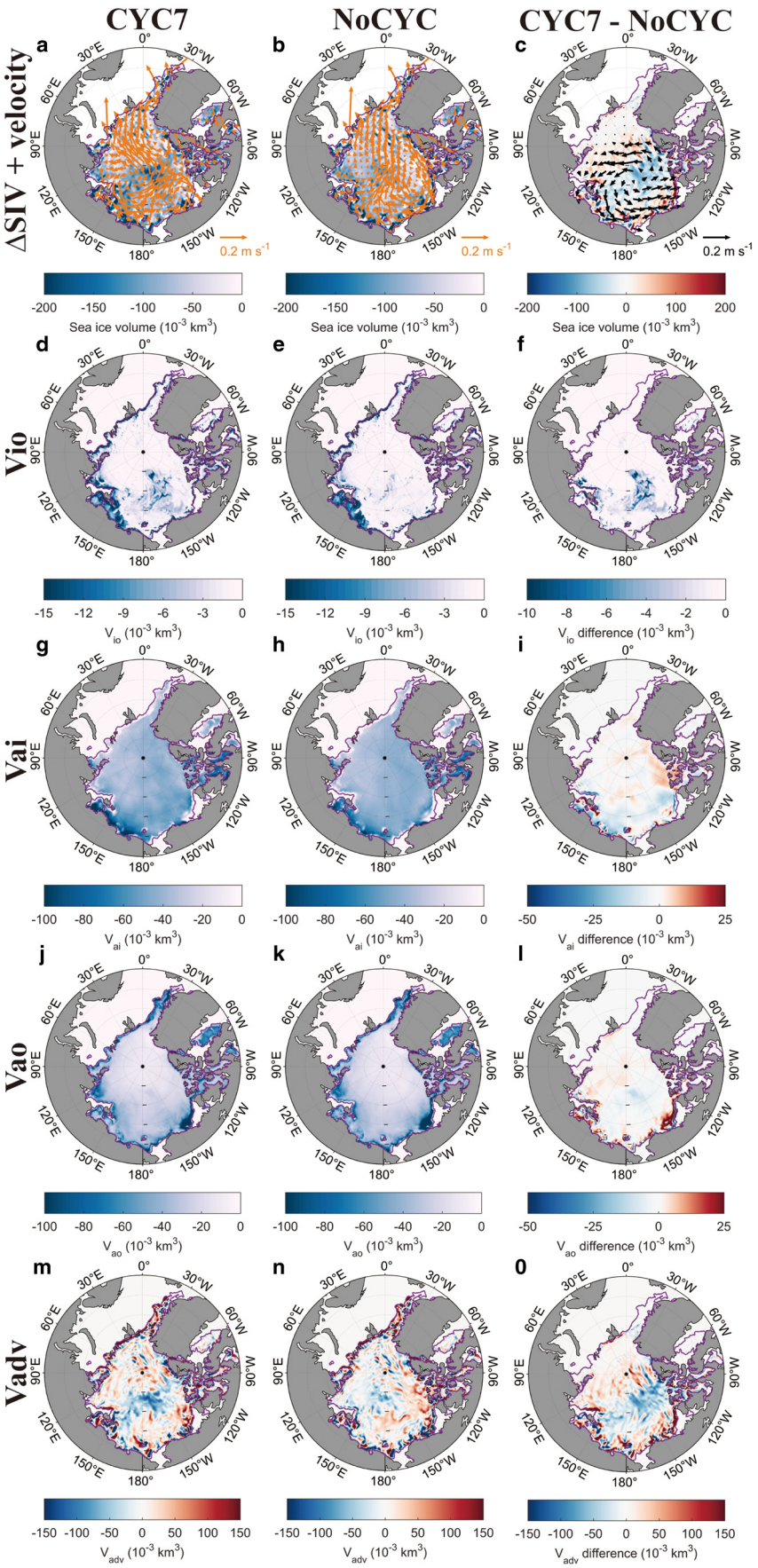

Figure 5. Spatial distributions of the integrated ΔSIV and mean sea-ice velocity (first row), the integrated V_{io} (second row), V_{ai} (third row), V_{ao} (fourth row) and V_{adv} (fifth row) during the active period of the cyclone in the CYC7 run (first column), the NoCYC run (second column) and their differences (third column). The purple lines represent the mean sea-ice edge during the active period of the cyclone in the CYC7 run. Note the various colorbars in different panels.

https://doi.org/10.1017/aog.2024.15 Published online by Cambridge University Press

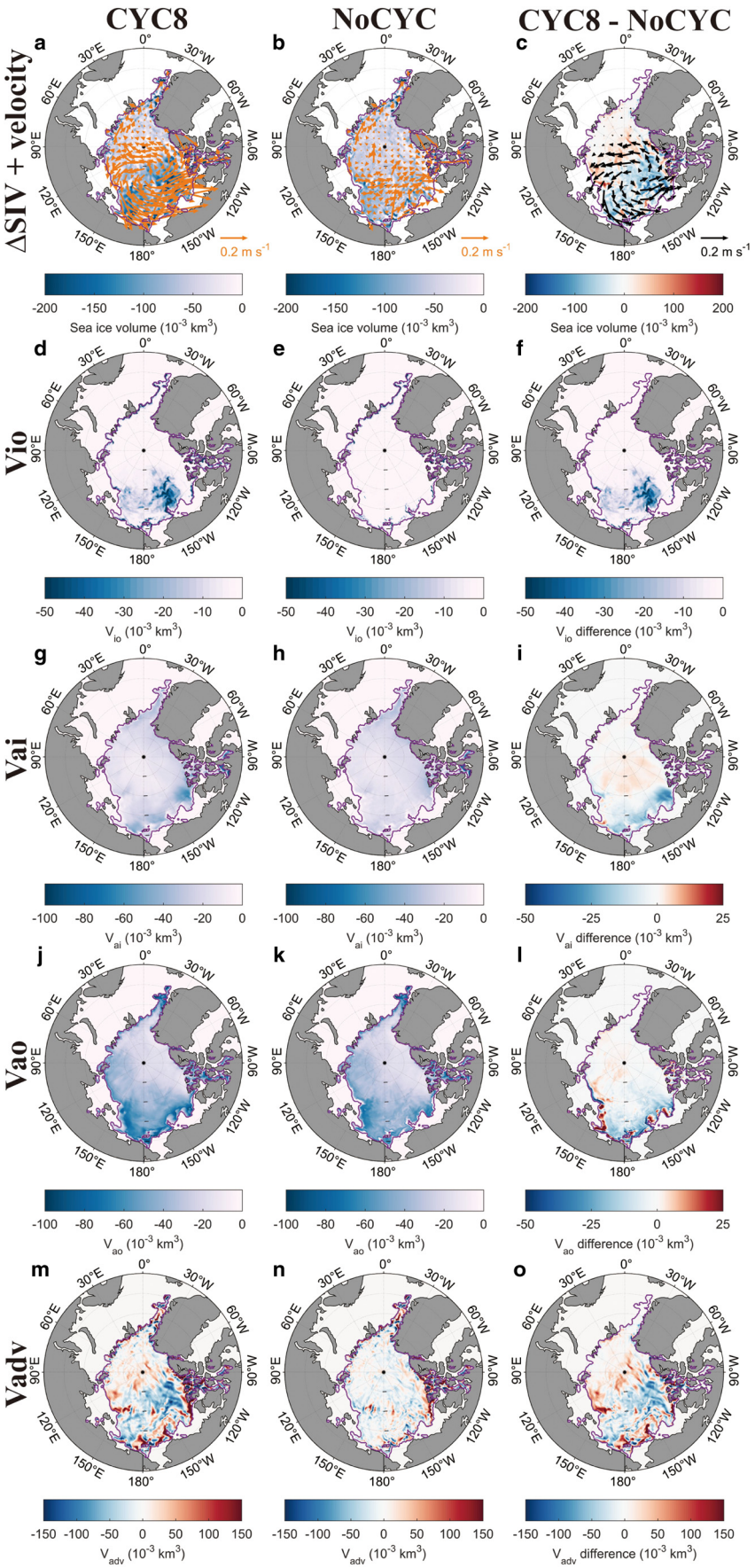

Figure 6. Spatial distributions of the integrated ΔSIV and mean sea-ice velocity (first row), the integrated V_{io} (second row), V_{ai} (third row), V_{ao} (fourth row) and V_{adv} (fifth row) during the active period of the cyclone in the CYC8 run (first column), the NoCYC run (second column) and their differences (third column). The purple lines represent the mean sea-ice edge during the active period of the cyclone in the CYC8 run. Note the various colorbars in different panels.

https://doi.org/10.1017/aog.2024.15 Published online by Cambridge University Press

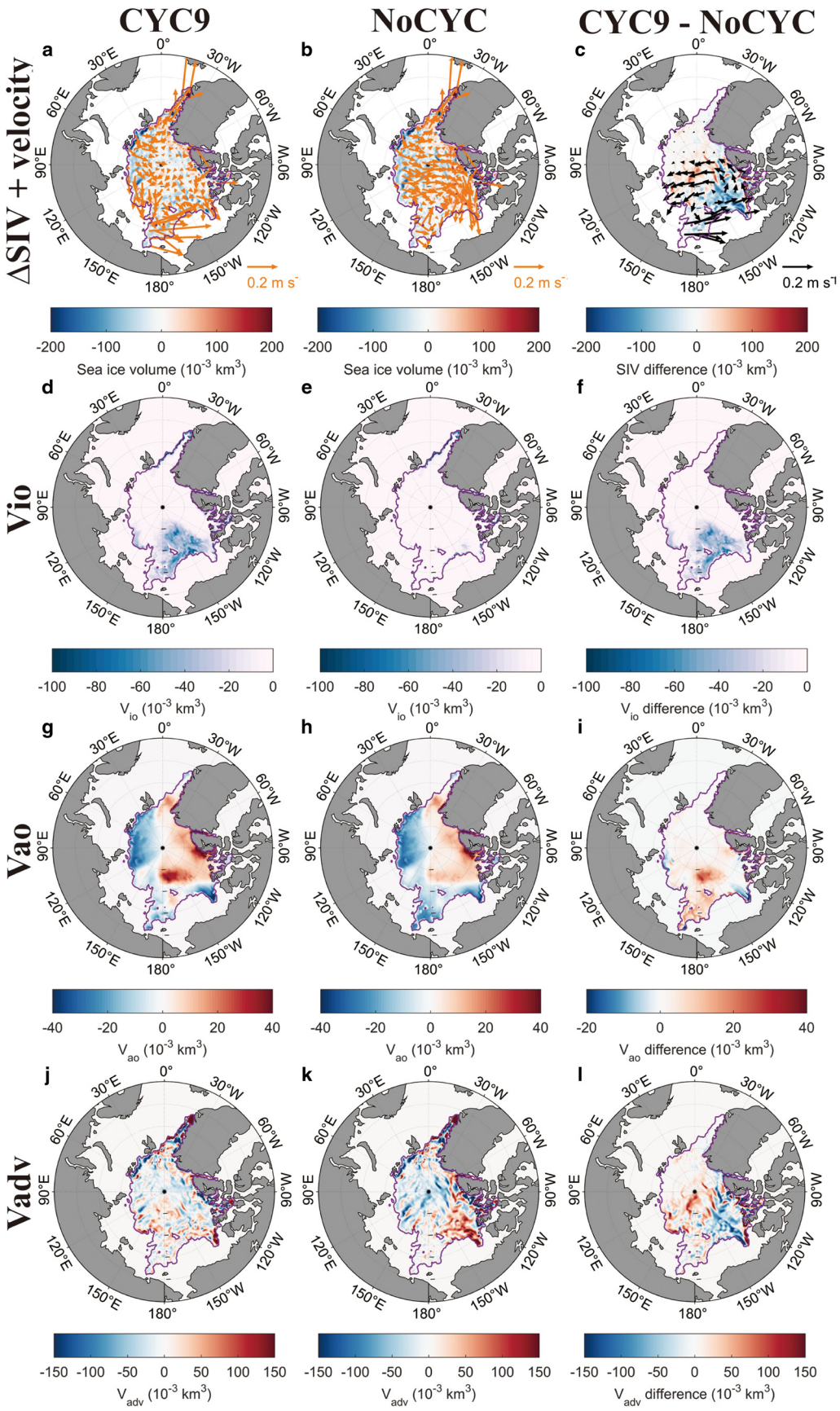

Figure 7. Spatial distributions of the integrated ΔSIV and mean sea-ice velocity (first row), the integrated V_{io} (second row), V_{ao} (third row) and V_{adv} (fourth row) during the active period of the cyclone in the CYC9 run (first column), the NoCYC run (second column) and their differences (third column). The purple lines represent the mean sea-ice edge during the active period of the cyclone in the CYC9 run. Note the various colorbars in different panels.

https://doi.org/10.1017/aog.2024.15 Published online by Cambridge University Press

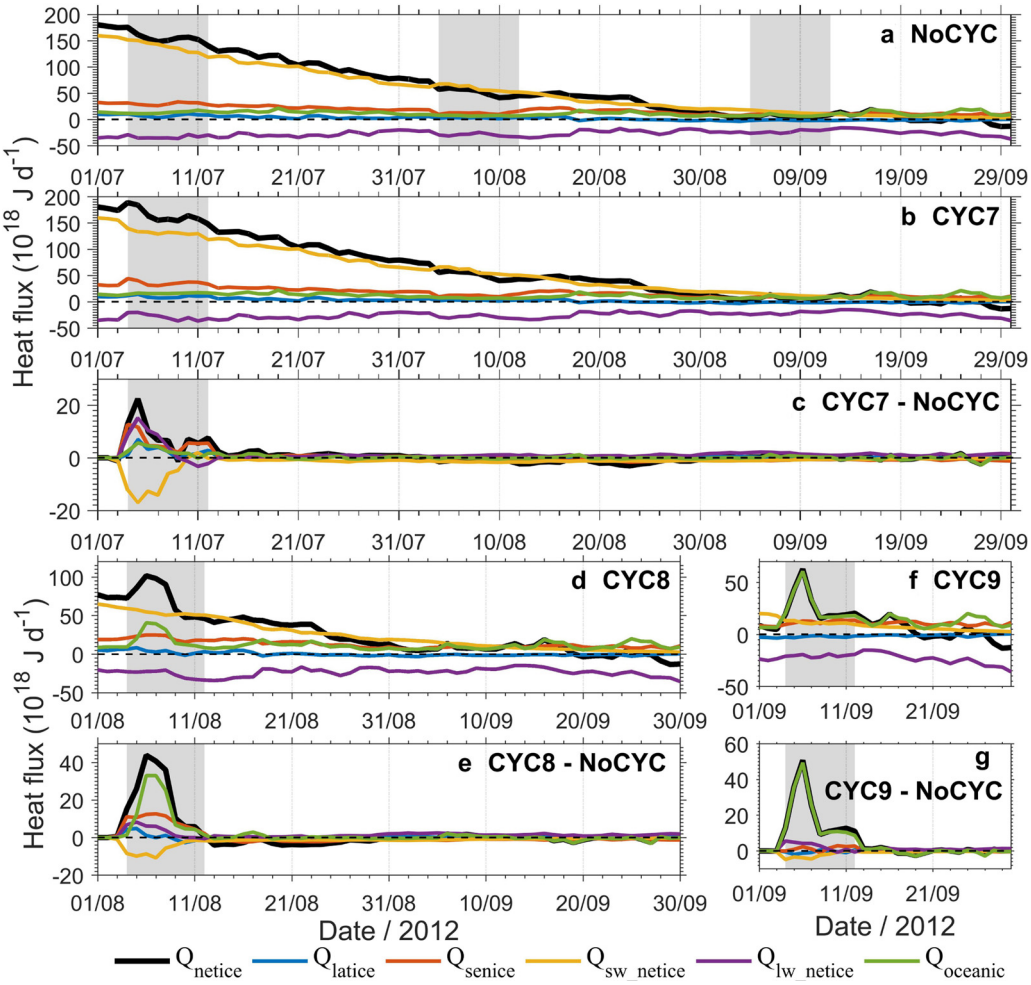

Figure 8. Time series of the heat flux budget terms over ice-covered area in (a) the NoCYC run, (b) the CYC7 run, (d) the CYC8 run, (f) the CYC9 run and the differences between (c) the CYC7, (e) the CYC8, (g) the CYC9 and the NoCYC runs. The black, blue, orange, yellow, purple and green lines denote the Q_{netice}, Q_{latice}, Q_{senice}, Q_{sw_netice}, Q_{lw_netice} and $Q_{oceanic}$, respectively. The active period of the cyclone is shaded by light gray. Positive value means heat absorbed by sea ice/open water. Positive values in (c), (e) and (g) mean that the heat absorbed by sea ice in the CYC7, CYC8 and CYC9 runs is larger than that in the NoCYC run, respectively.

at the ice surface, latent heat flux at the ice surface, sensible heat flux at the ice surface and oceanic heat flux at the ice bottom, respectively. The terms with subscripts 'ocn' instead of 'ice' denote the heat fluxes are computed over the open water area in the sea-ice zone. The heat flux absorbed by sea ice/open water in the sea-ice zone is positive.

In the ice-covered area, large changes happen in all heat budget terms during the active period of the cyclone for all the runs with the cyclone, while no significant changes occur in other periods (Fig. 8). Normally cyclones bring cloudy sky condition, thus shortwave radiation heat flux arriving at the ice surface greatly attenuates in all the runs with the cyclone (yellow lines in Figs 8c, e, g). In the CYC7 run, all the rest of the terms are larger than the corresponding terms in the NoCYC run, especially the longwave radiation and sensible heat fluxes (Fig. 8c). Comparing the CYC7 and NoCYC runs, the deviations in the radiation heat flux (shortwave plus longwave radiation heat fluxes) and turbulent heat flux (latent plus sensible heat fluxes) reach -0.70×10^{18} and 2.20×10^{18} J d^{-1} during the active period of the cyclone, respectively. In other words, when the cyclone occurs in July, the change of V_{ai} is mainly dominated by the turbulent heat flux, resulting from the fact that the enhanced mixture of warm and moist air within the atmospheric boundary layer caused by the cyclone-induced strong wind anomaly leads to more heat transfer from air to ice to elevate sea-ice surface melt. The oceanic heat flux contributes the largest deviation to the net heat flux in the ice-covered area between the CYC8 and NoCYC runs (green line in Fig. 8e), with an average increment of 3.38×10^{18} J d^{-1} during the active period of the cyclone. Comparing to the NoCYC run, enhancements are found in the latent, sensible, and longwave radiation heat fluxes in the CYC8 run. The summary of these positive deviations with an average of 3.21×10^{18} J d^{-1}, overcomes the negative deviation in the shortwave radiation heat flux with an average of -1.47×10^{18} J d^{-1}. The turbulent heat flux still is the main contributor in the enhancement of V_{ai} in the CYC8 run. Oceanic heat flux dominates net heat flux in the ice-covered area during the active period of the cyclone between the CYC9 and NoCYC runs (green line in Fig. 9g), while changes in other budget terms are quite small, indicating that only sea-ice bottom melt is promoted when the cyclone occurs in early September.

The evolution of V_{ao} relates to the net heat flux in the open water area in the ice zone. Comparing the CYC7 and NoCYC runs shows that the decrease in the shortwave radiation heat flux dominates the deviation in the Q_{netocn} (Fig. 9c), while the slight increases in the latent, sensible and longwave radiation heat fluxes cannot offset the strong decrease in the shortwave radiation heat flux during 4–9 July, thus the cyclone-induced net heat flux change in the open water area in the ice zone tends to impede sea-ice melt during 4–9 July. Thereafter, open

https://doi.org/10.1017/aog.2024.15 Published online by Cambridge University Press

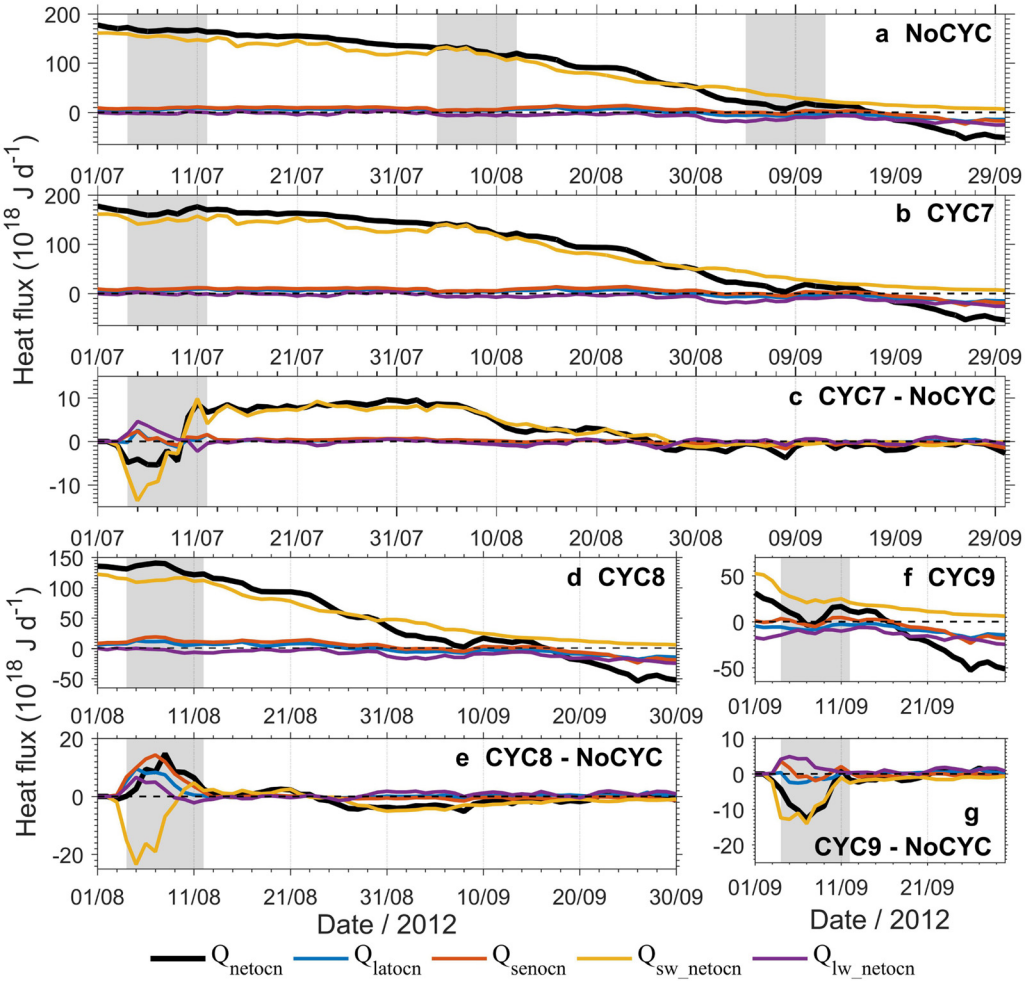

Figure 9. Time series of the heat flux budget terms over open water area in the sea-ice zone in (a) the NoCYC run, (b) the CYC7 run, (d) the CYC8 run, (f) the CYC9 run and the differences between (c) the CYC7, (e) the CYC8, (g) the CYC9 and the NoCYC runs. The black, blue, orange, yellow and purple lines denote the Q_{netocn}, Q_{latocn}, Q_{senocn}, Q_{sw_netocn} and Q_{lw_netocn}, respectively. The active period of the cyclone is shaded by light gray. Positive value means heat absorbed by sea ice/open water. Positive values in (c), (e) and (g) mean that the heat absorbed by open water within ice zone in the CYC7, CYC8 and CYC9 runs is larger than that in the NoCYC run, respectively.

water area in the ice zone in the CYC7 run expands more quickly than that in the NoCYC run (Fig. 3e), allowing more shortwave heat flux to arrive the open water area, and thus promoting the positive snow/ice albedo feedback and enhanced sea-ice melt. Comparing the CYC8 and NoCYC runs shows that the cyclone-induced increase in the rest of the budget terms overcomes the decrease in the shortwave heat flux during the active period of the cyclone (Fig. 8e), leading to that V_{ao} positively contributes to SIV loss. The changes of heat budget terms in the CYC9 run (Fig. 8g) are basically similar to those in the CYC7 run.

From the above analysis, we realize that the cyclone-associated changes of V_{io}, V_{ai} and V_{ao} are primarily dominated by the oceanic heat flux at the ice bottom ($Q_{oceanic}$), the turbulent heat flux at the air–ice interface ($Q_{latice} + Q_{senice}$) and the turbulent heat flux at the air–ocean interface ($Q_{latocn} + Q_{senocn}$), respectively. The net heat flux in the sea-ice zone ($Q_{net} = Q_{netice} + Q_{netocn}$) of the Pacific Arctic in the CYC7 run is larger than that in the NoCYC run (Figs 10a, e, i). In the CYC7 run, enhanced oceanic heat flux mainly occurs in the Chukchi Cap and the northern Canadian Basin (Fig. 10j), increased turbulent heat flux in the open water area in the ice zone mainly occurs in the East Siberian Sea and northern Beaufort Sea (Fig. 10k), and enhanced turbulent heat flux in the ice-covered area mainly occurs in areas near to the cyclone's trajectory (Fig. 10l). Comparing the CYC8 and NoCYC runs shows that a relatively large increase in the Q_{net} happens in the marginal ice zone in the Pacific Arctic (Fig. 11i), enhanced oceanic heat flux occurs in the northwestern Beaufort Sea (Fig. 11j) and strengthened turbulent heat exchange between ocean, ice and atmosphere also occurs in the marginal ice zone in the Pacific Arctic (Figs 11k, l). With respect to the NoCYC run, the CYC9 run produces larger $Q_{oceanic}$ in the East Siberian Sea and northern Canadian Basin (Fig. 12f).

4. Discussion and conclusions

This paper focuses on the influence of the timing of an extreme cyclone on the Arctic summertime SIV evolution based on the Arctic Ice Ocean Prediction System. We use a novel cyclone removal algorithm (Tian and others, 2022) to isolate the extreme cyclone that occurred in August 2012 from the background atmospheric state in the JRA55 data. Different from previous studies on this topic, we move the cyclone occurrence to other months to assess the importance of seasonal timing. By removing the extreme cyclone or superimposing it onto the atmospheric state one month earlier or later, sea ice and heat flux budget analysis are conducted based on four numerical experiments driven by the original or modified JRA55 data. The

https://doi.org/10.1017/aog.2024.15 Published online by Cambridge University Press

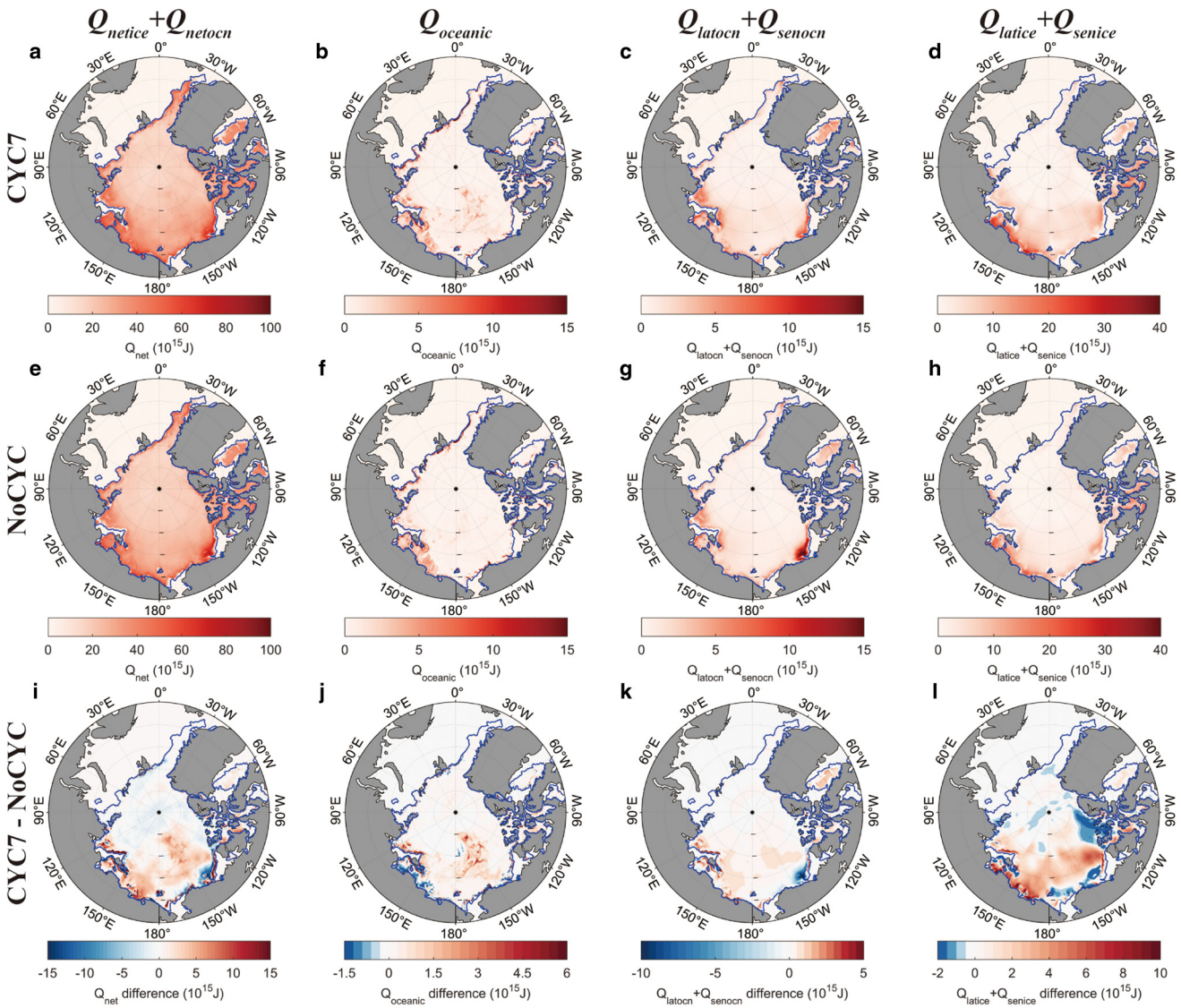

Figure 10. Spatial distributions of integrated $Q_{netice} + Q_{netocn}$ (Q_{net}, first column), $Q_{oceanic}$ (second column), $Q_{latocn} + Q_{senocn}$ (third column) and $Q_{latice} + Q_{senice}$ (fourth column) during the active period of the cyclone. The top, middle, bottom rows denote the CYC7 run, the NoCYC run, and the differences between the CYC7 and NoCYC runs, respectively. The blue lines represent the mean sea-ice edge during the active period of the cyclone in the CYC7 run. Note the various colorbars in different panels.

extreme cyclone happened in August, and SIV loss occurred at the ice bottom primarily and the ice surface secondarily, resulting from enhanced oceanic heat flux at the ice base and elevated turbulent heat fluxes between air and ice/ocean surface in the sea-ice zone. Strong SIV reduction occurs in the marginal ice zone of the Pacific Arctic, specifically the east side of the trajectory of the cyclone center (Figs 1a, 6c). Enhanced ice bottom melt occurred in the northwestern Beaufort Sea, and enhanced ice surface melt occurred in the marginal ice zone in the East Siberian–Chukchi–Beaufort Seas. This conclusion is basically in line with most previous studies on the topic of impacts of the extreme cyclone in August 2012 on the Arctic sea ice, e.g. Zhang and others (2013), Stern and others (2020), Lukovich and others (2021), Tian and others (2022) and Clancy and others (2022).

Noticeably, our study further finds that although the extreme cyclone leads to strong SIV loss in all experiments, large divergence exists in the melting mechanism in response to various timing of the cyclone, in which sea-ice condition prior to the extreme cyclone plays a vital role in affecting the cyclone-induced SIV evolution. If the cyclone occurs in July, ice surface melt dominates ice volume loss due to the cyclone-induced enhanced turbulent heat flux between air and ice surface, and ice bottom melt contributes to ice volume loss. The cyclone-associated enhanced sea-ice surface melt is primarily located in the East Siberian–Chukchi–Beaufort Seas while the cyclone-associated enhanced sea-ice bottom melt locates in the Chukchi Cap and the northern Canadian Basin. Compared with the August cyclone, relatively higher ice concentration in July likely damps the cyclone's momentum export into the Arctic Ocean, impedes the elevation of oceanic mixing level and thus leads to weaker ice bottom melt. However, the July cyclone leads to early appearance of open water area in the sea-ice zone, which initiates the positive snow/ice albedo feedback, causes more solar heat absorbed by the ocean, and results in enhanced sea-ice melt in the following one month. If the cyclone occurs in September, SIV loss is almost entirely attributed to ice bottom melt, and the cyclone-associated heat exchange between air and open water area in the sea-ice zone leads to SIV gain in contrast. Finocchio and others (2022), Finocchio and Doyle (2021) found that cyclones earlier in the melt season (June) tend to impede sea-ice loss while cyclones later in the melt season (August) tend to accelerate sea-ice loss

https://doi.org/10.1017/aog.2024.15 Published online by Cambridge University Press

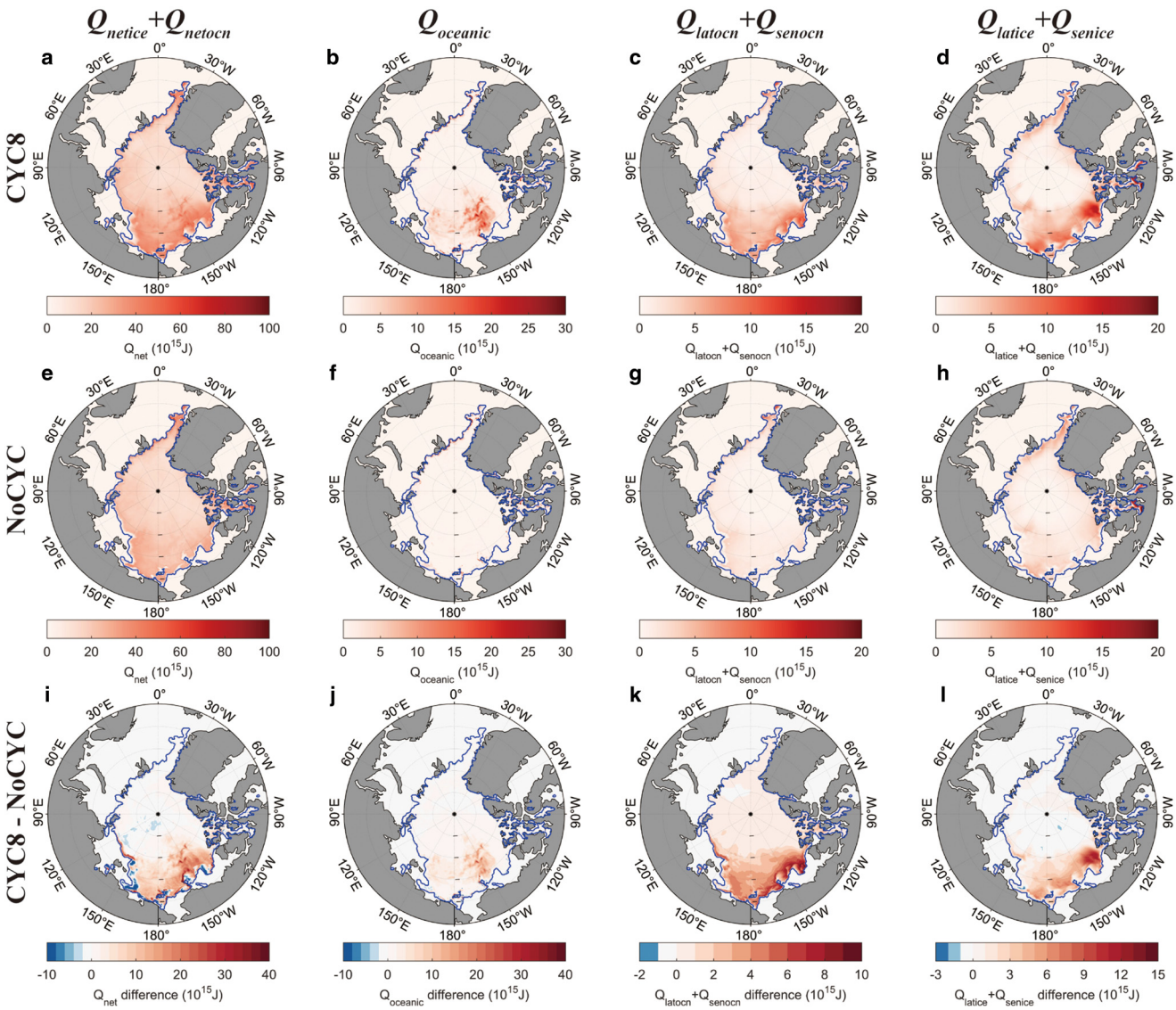

Figure 11. Same as Fig. 10, but for the CYC8 run.

through statistical analysis. Our result shows that enhanced SIV losses are induced by the extreme cyclone whether it occurs in July, August or September. The divergence of the conclusions originates partly from our study that cyclone is an extreme one, partly from that the July case is possibly different from the June cyclone.

It should be pointed out that most of the above-mentioned analysis focused on pan-Arctic SIV evolution and omitted regional SIV differentiation induced by the cyclone's dynamical impacts on sea ice, such as sea-ice advection and deformation. The cyclone's thermodynamical influence decides pan-Arctic SIV evolution; however, the cyclone's dynamical influence contributes, even dominates, regional SIV distribution (Figs 5o, 6o, 7o). Clancy and others (2022) found that the dynamical and thermodynamical responses of SIC to cyclones are comparable in magnitude, and the dynamical processes dominate the response of sea-ice thickness and are the primary driver of the east–west difference in the sea-ice response to cyclones. Similar finding can be concluded from our results, essentially the selected extreme cyclone in August 2012 in the present study is pronounced in highlighting sea-ice dynamical responses. Schreiber and Serreze (2020) suggested that SIC in the following several days is higher with cyclone than that without cyclone, as SIC decrease induced by sea-ice dynamical response is outweighed by SIC increase induced by sea-ice thermodynamical response. Our analysis also suggests that an extreme cyclone occurring in July likely leads to a greater sea-ice extent in early August but a lower SIV minimum in September compared with those occurring in August or September (Fig. 3e). It should be mentioned that an ice–ocean coupled model lacking the feedback from sea ice/ocean to atmosphere may underestimate the sensible heat flux at the sea ice–atmosphere interface comparing with an ice–ocean–atmosphere coupled model (Stern and others, 2020). Therefore, in our study with prescribed atmospheric forcing, the September SIV minimum in the July cyclone is still overestimated.

The relationship between the extreme cyclone in August 2012 and sea-ice loss have been extensively studied, using ice–ocean coupled model (Zhang and others, 2013) and air–ice–ocean coupled model (Stern and others, 2020). Our results generally confirm previous findings. As a contributor to the community knowledge of Arctic cyclones and sea ice, in this work we purpose a new numerical method to disentangle the influences of the timing of cyclones on sea-ice evolution. In our plan, a high-resolution ice–ocean model with advanced performance on sea-ice rheology and more sophisticated cyclone tracking/removal algorithms is scheduled to further contribute knowledge to the Arctic scientific community on this topic.

https://doi.org/10.1017/aog.2024.15 Published online by Cambridge University Press

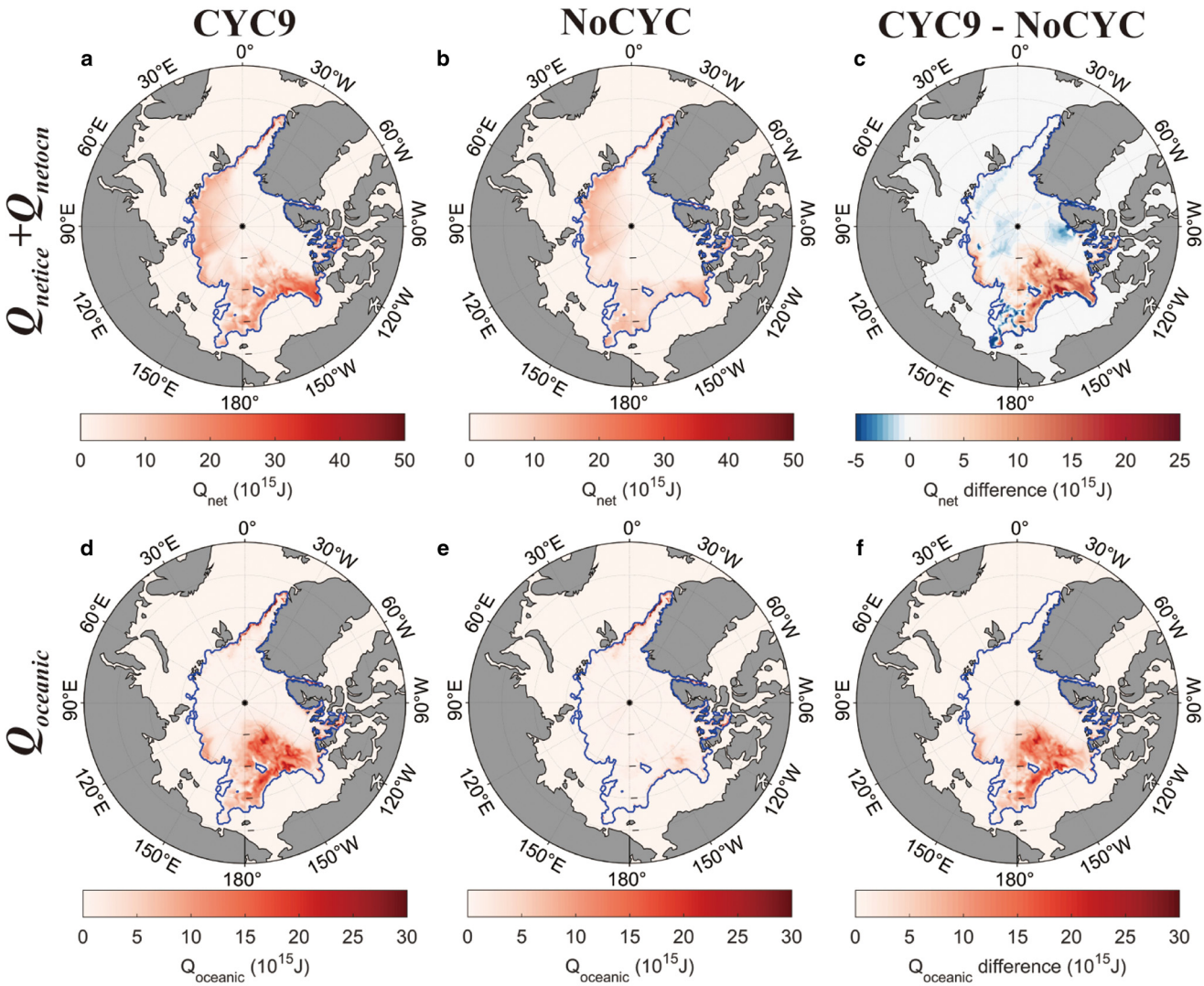

Figure 12. Spatial distributions of integrated $Q_{netice} + Q_{netocn}$ (Q_{net}, first row) and $Q_{oceanic}$ (second row) during the active period of the cyclone. The left, middle, right columns denote the CYC9 run, the NoCYC run, and the differences between the CYC9 and NoCYC runs, respectively. The blue lines represent the mean sea-ice edge during the active period of the cyclone in the CYC9 run. Note the various colorbars in different panels.

Supplementary material. The supplementary material for this article can be found at https://doi.org/10.1017/aog.2024.15

Acknowledgments. The authors thank Scientific Editor David Babb and Associate Chief Editor Christian Haas for handling the manuscript, and three anonymous reviewers are thanked for constructive comments. This work is supported by the National Natural Science Foundation of China (42276250), and the National Key R&D Program of China (2022YFF0802000).

Data availability. The JRA-55 data are available from the Japan Meteorological Agency (http://search.diasjp.net/en/dataset/JRA55). The SSMIS and SMOS data are available from the University of Hamburg (https://icdc.cen.uni-hamburg.de/thredds/aggregationSsmiAsiCatalog.html; http://icdc.cen.uni-hamburg.de/1/daten/cryosphere/l3c-smos-sit.html). The Cryosat-2 data are available from the Alfred-Wegener-Institut, Helmholtz Zentrum für Polar- und Meeresforschung (http://data.meereisportal.de/data/cryosat2/version2.0/). The GMPE SST data are available from the Copernicus Marine Environment Monitoring Service (http://marine.copernicus.eu/).

References

Aue L and Rinke A (2023) Cyclone impacts on sea ice concentration in the Atlantic Arctic ocean: annual cycle and recent changes. *Geophysical Research Letters* **50**, e2023GL104657. doi: 10.1029/2023GL104657

Bi H and 7 others (2018) Arctic sea ice volume changes in terms of age as revealed from satellite observations. *IEEE Journal of Selected Topics in Applied Earth Observations and Remote Sensing* **11**(7), 2223–2237. doi: 10.1109/JSTARS.2018.2823735

Cavalieri DJ, Parkinson CL, DiGirolamo N and Ivanoff A (2011) Intersensor calibration between F13 SSMI and F17 SSMIS for global sea ice data records. *IEEE Geoscience and Remote Sensing Letters* **9**(2), 233–236. doi: 10.1109/LGRS.2011.2166754

Clancy R, Bitz CM, Blanchard-Wrigglesworth E, McGraw MC and Cavallo SM (2022) A cyclone-centered perspective on the drivers of asymmetric patterns in the atmosphere and sea ice during Arctic cyclones. *Journal of Climate* **35**(1), 73–89. doi: 10.1175/JCLI-D-21-0093.1

Daru V and Tenaud C (2004) High order one-step monotonicity-preserving schemes for unsteady compressible flow calculations. *Journal of Computational Physics* **193**(2), 563–594. doi: 10.1016/j.jcp.2003.08.023

Doney SC, Large WG and Bryan FO (1998) Surface ocean fluxes and water-mass transformation rates in the coupled NCAR climate system model. *Journal of Climate* **11**, 1420–1441. doi: 10.1175/1520-0442(1998)011<1420:sofawm>2.0.co; 2

Finocchio PM and Doyle JD (2021) Summer cyclones and their association with short-term sea ice variability in the pacific sector of the arctic. *Frontiers in Earth Science* **9**, 738497. doi: 10.3389/feart.2021.738497

Finocchio PM, Doyle JD, Stern DP and Fearon MG (2020) Short-term impacts of Arctic summer cyclones on sea ice extent in the marginal ice zone. *Geophysical Research Letters* **47**, e2020GL088338. doi: 10.1029/2020GL088338

Finocchio PM, Doyle JD and Stern DP (2022) Accelerated sea-ice loss from late-summer cyclones in the New Arctic. *Journal of Climate* **35**(23), 7751–7769. doi: 10.1175/jcli-d-22-0315.1

Graham RM and 28 others (2019) Winter storms accelerate the demise of sea ice in the Atlantic sector of the Arctic Ocean. *Scientific Report* **9**, 9222. doi: 10.1038/s41598-019-45574-5

Hao G, Su J, Vihma T and Huang F (2020) Trends, abrupt shifts and inter-annual variability of the Arctic wintertime seasonal sea ice from 1979 to 2019. *Annals of Glaciology* **61**(83), 441–453. doi: 10.1017/aog.2020.68

Hibler III WD (1980) Modeling a variable thickness sea ice cover. *Monthly Weather Review* **108**(12), 1943–1973. doi: 10.1175/1520-0493(1980)108<1943:MAVTSI>2.0.CO;2

Jackson JM, Williams WJ and Carmack EC (2012) Winter sea-ice melt in the Canada Basin, Arctic Ocean. *Geophysical Research Letters* **39**, L03603. doi: 10.1029/2011GL050219

Kaleschke L and 6 others (2001) SSM/I sea ice remote sensing for mesoscale ocean-atmosphere interaction analysis. *Canadian Journal of Remote Sensing* **27**(5), 526–537. doi: 10.1080/07038992.2001.10854892

Kriegsmann A and Brümmer B (2014) Cyclone impact on sea ice in the central Arctic Ocean: a statistical study. *The Cryosphere* **8**(1), 303–317. doi: 10.5194/tc-8-303-2014

Kwok R (2018) Arctic sea ice thickness, volume, and multiyear ice coverage: losses and coupled variability (1958–2018). *Environmental Research. Letters* **13**(10), 105005. doi: 10.1088/1748-9326/aae3ec

Large WG, McWilliams JC and Doney SC (1994) Oceanic vertical mixing: a review and a model with a nonlocal boundary layer parameterization. *Review of Geophysics* **32**(4), 363–403. doi: 10.1029/94RG01872

Laxon SW and 14 others (2013) CryoSat-2 estimates of Arctic sea ice thickness and volume. *Geophysical Research Letters* **40**(4), 732–737. doi: 10.1002/grl.50193

Liang X, Zhao F, Li C, Zhang L and Li B (2020) Using sea surface temperature observations to constrain upper ocean properties in an Arctic sea ice-ocean data assimilation system. *Journal of Geophysical Research: Oceans* **124**, 4727–4743. doi: 10.1029/2019JC015073

Liang X and 4 others (2020) Evaluation of ArcIOPS sea ice forecasting products during the ninth CHINARE-Arctic in summer 2018. *Advances in Polar Science* **31**(1), 14–25. doi: 10.13679/j.advps.2019.0019

Liang X and 7 others (2022) A comparison of factors that led to the extreme sea ice minima in the twenty-first century in the Arctic Ocean. *Journal of Climate* **35**(4), 1249–1265. doi: 10.1175/JCLI-D-21-0199.1

Lukovich JV and 6 others (2021) Summer extreme cyclone impacts on Arctic sea ice, *Journal of Climate* **34**(12), 4817–4834. doi: 10.1175/JCLI-D-19-0925.1

Marshall J, Adcroft A, Hill C, Perelman L and Heisey C (1997) A finite-volume, incompressible Navier Stokes model for studies of the ocean on parallel computers. *Journal of Geophysical Research: Oceans* **102**(C3), 5753–5766. doi: 10.1029/96JC02775

Martin M and 14 others (2012) Group for High Resolution Sea Surface temperature (GHRSST) analysis fields inter-comparisons. Part 1: a GHRSST multi-product ensemble (GMPE). *Deep Sea Research Part II* **77–80**, 21–30. doi: 10.1016/j.dsr2.2012.04.013

Mu L, Liang X, Yang Q, Liu J and Zheng F (2019) Arctic Ice Ocean Prediction System: evaluating sea-ice forecasts during Xuelong's first trans-Arctic Passage in summer 2017. *Journal of Glaciology* **65**(253), 813–821. doi: 10.1017/jog.2019.55

Nerger L, Janjić T, Schröter J and Hiller W (2012) A unification of ensemble square root Kalman filters. *Monthly Weather Review* **140**(7), 2335–2345. doi: 10.1175/MWR-D-11-00102.1

Ricker R, Hendricks S, Helm V, Skourup H and Davidson M (2014) Sensitivity of CryoSat-2 Arctic sea-ice freeboard and thickness on radar-waveform interpretation. *The Cryosphere* **8**(4), 1607–1622. doi: 10.5194/tc-8-1607-2014

Schreiber EA and Serreze MC (2020) Impacts of synoptic-scale cyclones on Arctic sea-ice concentration: a systematic analysis. *Annals of Glaciology* **61**(82), 139–153. doi: 10.1017/aog.2020.23

Screen JA, Simmonds I and Keay K (2011) Dramatic interannual changes of perennial Arctic sea ice linked to abnormal summer storm activity. *Journal of Geophysical Research: Atmosphere* **116**, D15. doi: 10.1029/2011JD015847

Semenov A, Zhang X, Rinke A, Dorn W and Dethloff K (2019) Arctic intense summer storms and their impacts on sea ice – A regional climate modeling study. *Atmosphere* **10**(4), 218. doi: 10.3390/atmos10040218

Serreze MC and 9 others (2003) A record minimum arctic sea ice extent and area in 2002. *Geophysical Research Letters* **30**(3), 1110. doi: 10.1029/2002GL016406

Simmonds I and Rudeva I (2012) The great Arctic cyclone of August 2012. *Geophysical Research Letters* **39**, 23. doi: 10.1029/2012GL054259

Simmonds I and Li M (2021) Trends and variability in polar sea ice, global atmospheric circulations, and baroclinicity. *Annals of the New York Academy of Sciences* **150**(4), 167–186. doi: 10.1111/nyas.14673

Stern D and 5 others (2020) The impact of an intense cyclone on short-term sea ice loss in a fully coupled atmosphere-ocean-ice model. *Geophysical Research Letters* **47**, e2019GL085580. doi: 10.1029/2019GL085580

Tian-Kunze X and 6 others (2014) SMOS-derived thin sea ice thickness: algorithm baseline, product specifications and initial verification. *The Cryosphere* **8**(3), 997–1018. doi: 10.5194/tc-8-997-2014

Tian Z and 5 others (2022) Thermodynamical and dynamical impacts of an intense cyclone on Arctic sea ice. *Journal of Geophysical Research: Oceans*, **127**, e2022JC018436. doi: 10.1029/2022JC018436

Zhang J and Rothrock DA (2003) Modeling global sea ice with a thickness and enthalpy distribution model in generalized curvilinear coordinates. *Monthly Weather Review* **131**(5), 845–861. doi: 10.1175/1520-0493(2003)131%3C0845:MGSIWA%3E2.0.CO;2

Zhang J, Lindsay R, Schweiger A and Steele M (2013) The impact of an intense summer cyclone on 2012 Arctic sea ice retreat. *Geophysical Research Letters* **40**(4), 720–726. doi: 10.1002/grl.50190

https://doi.org/10.1017/aog.2024.15 Published online by Cambridge University Press